



# Diagnosing Triggered Star Formation in the Galactic H II region Sh 2-142

Tanvi Sharma<sup>1</sup> , Wen Ping Chen<sup>1,2</sup> , Neelam Panwar<sup>3</sup> , Yan Sun<sup>4</sup> , and Yu Gao<sup>4,5</sup> <sup>1</sup>Institute of Astronomy, National Central University, 300 Zhongda Road, Zhongli 32001 Taoyuan, Taiwan<sup>2</sup>Department of Physics, National Central University, 300 Zhongda Road, Zhongli 32001 Taoyuan, Taiwan<sup>3</sup>Aryabhata Research Institute of Observational Sciences (ARIES), Manora Peak, Nainital 263 002, India<sup>4</sup>Purple Mountain Observatory, Chinese Academy of Sciences, 10 Yuanhua Road, Nanjing 210033, People's Republic of China<sup>5</sup>Department of Astronomy, Xiamen University, Xiamen, Fujian 361005, People's Republic of China

Received 2021 September 19; revised 2022 January 17; accepted 2022 January 31; published 2022 March 23

## Abstract

Stars are formed by gravitational collapse, spontaneously or, in some cases under the constructive influence of nearby massive stars, out of molecular cloud cores. Here we present an observational diagnosis of such triggered formation processes in the prominent H II region Sh 2-142, which is associated with the young star cluster NGC 7380, and with some bright-rimmed clouds as the signpost of photoionization of molecular cloud surfaces. Using near- (2MASS) and mid-infrared (WISE) colors, we identified candidate young stars at different evolutionary stages, including embedded infrared sources having spectral energy distributions indicative of active accretion. We have also used data from our optical observations to be used in SEDs, and from Gaia EDR3 to study the kinematics of young objects. With this young stellar sample, together with the latest CO line emission data (spectral resolution  $\sim 0.16 \text{ km s}^{-1}$ , sensitivity  $\sim 0.5 \text{ K}$ ), a positional and aging sequence relative to the neighboring cloud complex, and to the bright-rimmed clouds, is inferred. The propagating stellar birth may be responsible, at least partially, for the formation of the cluster a few million years ago, and for the ongoing activity now witnessed in the cloud complex.

*Unified Astronomy Thesaurus concepts:* [Star formation \(1569\)](#); [Star forming regions \(1565\)](#); [H II regions \(694\)](#); [Emission nebulae \(461\)](#); [Molecular gas \(1073\)](#); [Star clusters \(1567\)](#); [Open star clusters \(1160\)](#); [Young stellar objects \(1834\)](#); [Protostars \(1302\)](#)

## 1. Introduction

Massive stars, via their fierce radiation and stellar winds, have a profound effect on environments. The influence, on the one hand, could be destructive so as to disperse nearby molecular gas, quenching any further star formation activity. On the other hand, the OB stars may play a constructive role under certain circumstances (Elmegreen 1998; Lee & Chen 2007), with their winds giving “just the right touch” to sweep up the surrounding gas and dust to a dense shell that eventually fragments to form a group of young stars (the collect-and-collapse process, Elmegreen & Lada 1977). For a neighboring molecular clump, a luminous star may ionize the confronting surface layer, which manifests itself as a “bright-rimmed cloud” or a cometary globule, thereby sending inwards an implosive ionization shock front that squeezes the material and initiates cloud collapse, leading to the formation of the next-generation stars (the radiation driven implosion, Bertoldi 1989). More than spontaneous cloud collapse, such triggering mechanisms (Sugitani et al. 1989, 1991; Morgan et al. 2004) extend the star birth processes in time, producing stars at differing epochs in a cloud complex, and in length scales, propagating the formation sequence from one cloud to another.

The effect of OB stars on triggering the formation of next-generation stars in nearby molecular clouds would leave the following spatial and temporal prognostic trace (Chen et al. 2007): namely, (1) the remnant cloud is surrounding (in the collect-and-collapse scenario) or pointing to (if by the radiation driven mechanism) the OB stars; (2) the recently formed stellar groups

are aligned between the remnant cloud and the OB stars in an age sequence, with the younger population being nearer to the bright cloud rim, whereas the youngest ones, i.e., protostars, if any, are being formed inside the cloud.

The target of our study, the cloud complex Sh 2-142, shown in Figure 1, presents a likely case of triggered star formation. The H II region Sh 2-142 was first recognized by Caroline Herschel and later cataloged by Stewart Sharpless (Sharpless 1959). The principal ionizing star, DH Cep, is a spectroscopic binary (HD 215835, O5.5V+O6V) associated with the cluster NGC 7380 (C2245+578 in IAU nomenclature,  $\alpha = 22:47:16$ ,  $\delta = +58:07:30$ , J2000.0), which is at a heliocentric distance of 2.6 kpc and has an age of 4 Myr (Chen et al. 2011). This young, open cluster also fosters a pre-main-sequence (PMS) population (Baade 1983; Chen et al. 2011; Lata et al. 2016). The natal cloud embracing the cluster in the south and eastern side was revealed by molecular line observations (Israel 1978; Leisawitz et al. 1989). Furthermore, Joncas et al. (1988) disclosed two kinematically and spatially separated cores within the complex. The gas in the region has been dispersed by stellar winds and radiation, yet remains interacting with grouped young stellar objects (YSOs) (Koenig et al. 2012) and embedded far-infrared point sources.

The collation of far-infrared observations, H $\alpha$  imaging, radio continuum, and molecular line data (Joncas & Roy 1984; Joncas et al. 1985; Schwartz 1987; Chavarría-K et al. 1994) has revealed several peaks of density enhancement of molecular and ionized gas, thus uncovering the presence of peripheral bright rims that are likely to harbor very young stars. Indeed a few bright rims are present, including the extensively studied BRC 43, known to associate with embedded sources, which serves as a potential site for triggered star formation by the “radiatively driven implosion” mechanism (Sugitani et al. 1991; Morgan et al. 2008, 2010).

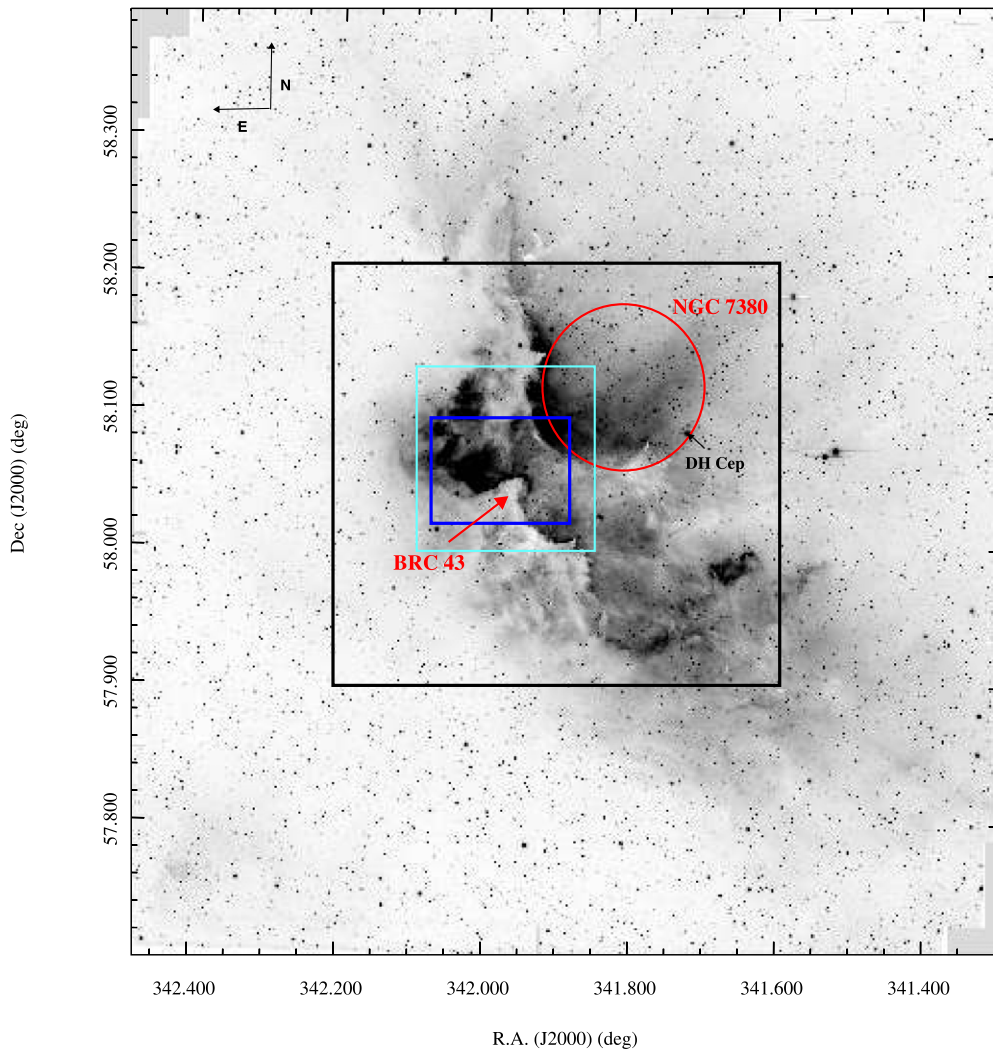


**Figure 1.** The Sh 2-142 complex of our study (color-inverted  $H\alpha$  image), where near- and mid-infrared data from 2MASS and WISE are analyzed. The black square marks the region in which deep optical  $BVI$  photometry from 1.3 m DFOT is available, and the cyan square for 2 m HCT, whereas the blue square is the region near BRC 43 within which  $H\alpha$  emission stars have been identified. The location of the cluster NGC 7380 is shown by a red circle and the principal ionizing star (DH Cep) for the region is labeled. The center for this image is at  $\alpha = 22:47:33.3$ ,  $\delta = +58:02:56.8$  (J2000).

In this paper we investigate the region to diagnose the star formation activity for the overall Sh 2-142 cloud complex, by associating the young population with the star cluster, as well as with the molecular and ionized gas. Combining near- and mid-infrared data, we update the list of young stars in the whole complex, including those still accreting mass, and collectively analyze their location and relative ages to gain insight into the influence of massive stars on the star formation history in neighboring molecular clouds. In the following, Section 2 describes the data used in this work, archival or otherwise acquired by ourselves, leading to Section 3 where the evolutionary status of the young objects is determined accordingly. Section 4 then presents the kinematics of young stars, and subsequently the interplay between parental molecular gas and YSOs. In Section 5 we discuss supporting evidence for, and limitations and uncertainties in our arguments, of influential star formation in this region.

## 2. Observations and Data Sources

Data used in this study consist of archival photometry in the infrared wavelengths, optical broadband imaging, and

molecular line observations. For infrared data, we have explored an area of  $\sim 38' \times 41'$  around NGC 7380 covering the entire cloud complex, exhibited in Figure 1, by exploiting the archival Two Micron All Sky Survey (2MASS) in  $J$  ( $1.25 \mu\text{m}$ ),  $H$  ( $1.65 \mu\text{m}$ ), and  $K_s$  ( $2.15 \mu\text{m}$ ) bands (Cutri et al. 2003), comprising a total of 18,316 point sources. In addition, the ALLWISE catalog (Cutri et al. 2013) is accessed for photometry at longer wavelengths (at  $3.4$ ,  $4.6$ ,  $12$ , and  $22 \mu\text{m}$ , respectively, named as W1, W2, W3, and W4 bands), appropriate for embedded sources. This data set consists of 9457 sources.

CCD imaging observations were carried out on 2018 October 6, using the Ritchey-Chretien Cassegrain 1.3 m telescope at Devasthal, Nainital, India, equipped with a back-illuminated, thermoelectrically cooled CCD camera assembled by ANDOR, with  $2048 \times 2048$  pixels. The  $BVI$  images were processed following the standard procedure with bias and flat-field corrections. Point spread function photometry was then performed using the IRAF/DAOPHOT-II analysis package. The Landolt standard field SA 92 was observed on the same night for photometric calibration. Additional deep  $BVI$  data was used toward BRC 43 taken in 2006 October with the 2 m

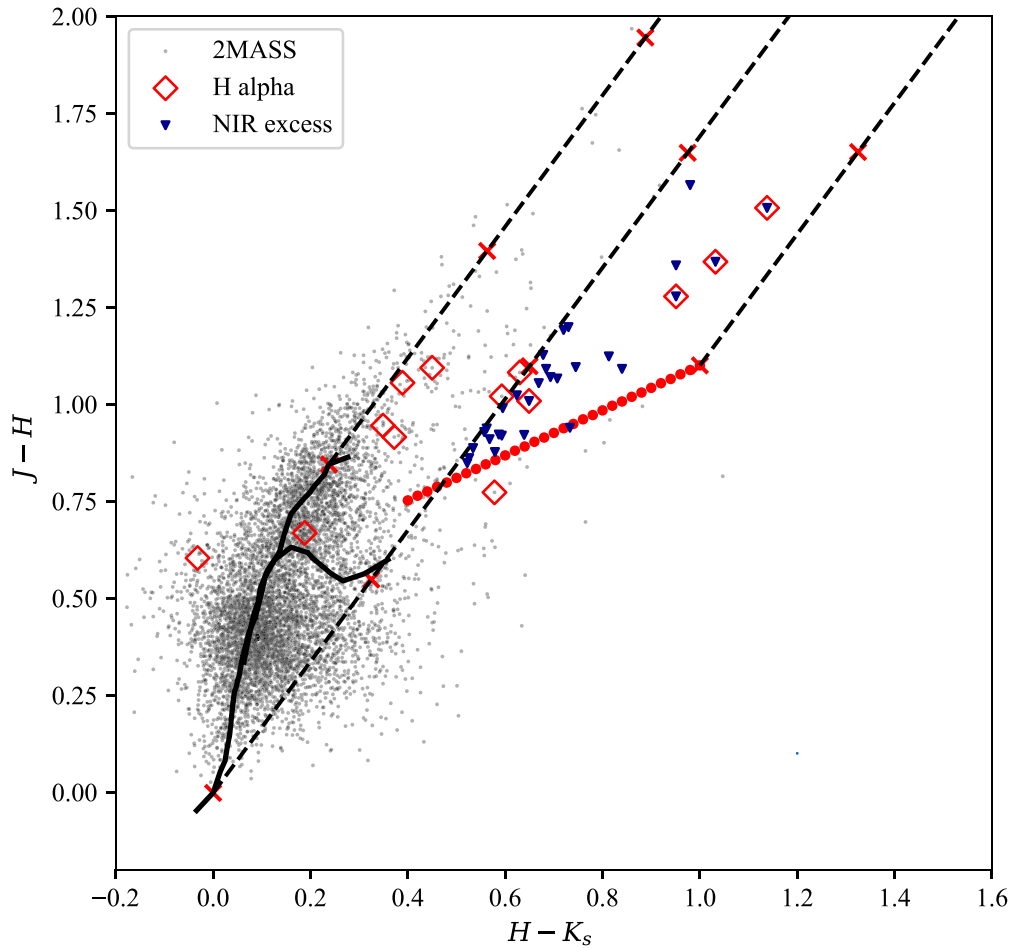


**Figure 2.** Near-infrared 2MASS  $J-H$  vs.  $H-K_s$  color-color diagram. The gray dots represent 2MASS measurements, whereas the black curves represent unreddened main-sequence and giant star loci (Bessell & Brett 1988). The intrinsic locus of classical T Tauri stars is marked by the dotted red line (Meyer et al. 1997). All the data are transformed to the CIT system (Carpenter 2001). Reddening vectors, shown as dotted black lines, adopting an interstellar law (Cohen et al. 1981) of  $A_J/A_V = 0.265$ ,  $A_H/A_V = 0.155$ , and  $A_K/A_V = 0.090$ , are drawn from the extreme tips of each locus, with the red crosses on each vector marking an increment of  $A_V=5$ . The red open diamond symbols mark  $H\alpha$  stars, whereas the blue filled symbols show infrared excess objects diagnosed in this diagram.

Himalayan Chandra Telescope (HCT) at Hanle, India, with the same data reduction procedure. The HCT observations are limited only to the BRC 43 region, and for overlapping regions by both telescopes, we adopted the results by the 1.3 m for the bright targets ( $V < 17$ ) mag and by the 2 m for fainter ( $V \geq 17$ ) ones.

The extinction coefficients in different filters for 1.3-m:  $K_U = 0.516 \pm 0.088$ ,  $K_B = 0.252 \pm 0.019$ ,  $K_V = 0.153 \pm 0.016$ , and  $K_I = 0.083 \pm 0.017$ . Transmission coefficient values are as follows:

$$\begin{aligned} U - B &= 0.938(U_0 - B_0) - 1.390 \\ B - V &= 1.215(B_0 - V_0) - 0.847 \\ V - I &= 0.917(V_0 - I_0) + 0.211 \\ V - V_0 &= -0.098(B - V) - 2.282 \\ B - B_0 &= 0.031(U - B) - 2.92. \end{aligned}$$

The extinction coefficients, transmission coefficients, and zero-points for the HCT are taken from Chauhan et al. (2009).

We have used the Gaia EDR3 data (Gaia Collaboration 2020) to analyze the kinematics of the young population in the same region as the archival infrared data and has 48,847 sources toward Sh 2-142, and utilize this data for parallax and proper motions.

The molecular gas is traced by  $^{12}\text{CO}$ ,  $^{13}\text{CO}$ , and  $\text{C}^{18}\text{O}$  emissions, all of  $J=1-0$  transitions, observed with the 13.7 m radio telescope at Delingha, China. The data are part of the long-term effort by the Purple Mountain Observatory nearly 10 yr ago to map the Galactic plane (Su et al. 2019). The data format is in three-dimensional cubes with two spatial axes (Galactic longitude and latitude) and one spectral axis (LSR velocity). For the  $^{12}\text{CO}$  emission at 115 GHz, the spectral resolution (channel width) is  $\sim 0.16 \text{ km s}^{-1}$  with a typical sensitivity of about 0.5 K. For  $^{13}\text{CO}$  and  $\text{C}^{18}\text{O}$  near 110 GHz, the resolution and typical sensitivity are, respectively,  $0.17 \text{ km s}^{-1}$  and  $\sim 0.3 \text{ K}$ . CO data toward Sh 2-142 have either subarcminute spatial resolution or high resolution ( $30''$ ) but are limited only to the vicinity of BRC 43 (Joncas et al. 1988). Our molecular line data cover the entire complex at an angular resolution of  $\sim 50''$  with a uniform sensitivity.

### 3. Identification of Young Stellar Objects

The young stellar sample gathered for this study includes those known to display emission lines in the spectra, and those that have characteristic infrared radiation in excess of photospheric radiation, originated from circumstellar dust emission, diagnosed by near- and mid-infrared colors.

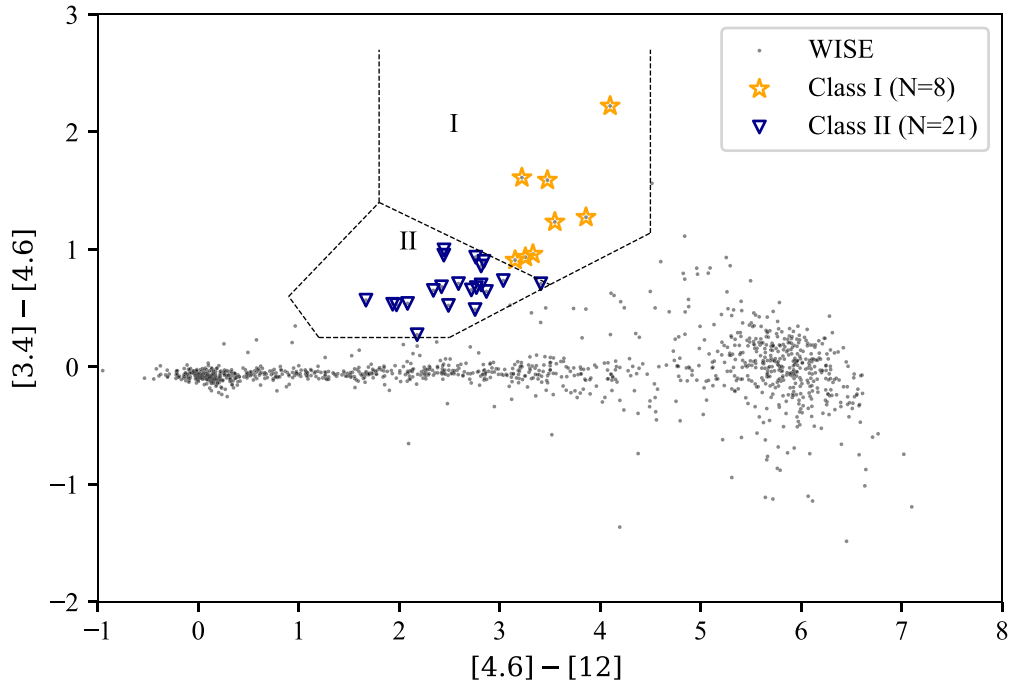


**Figure 3.** The WISE mid-infrared color-color diagram, from 3.4 to 12  $\mu\text{m}$ , to identify Class I objects (represented by orange asterisks) and Class II objects (open triangles in blue), following the selection criteria in Koenig & Leisawitz (2014). Gray dots mark all 1846 sources with the photometric quality flag “AAA.”

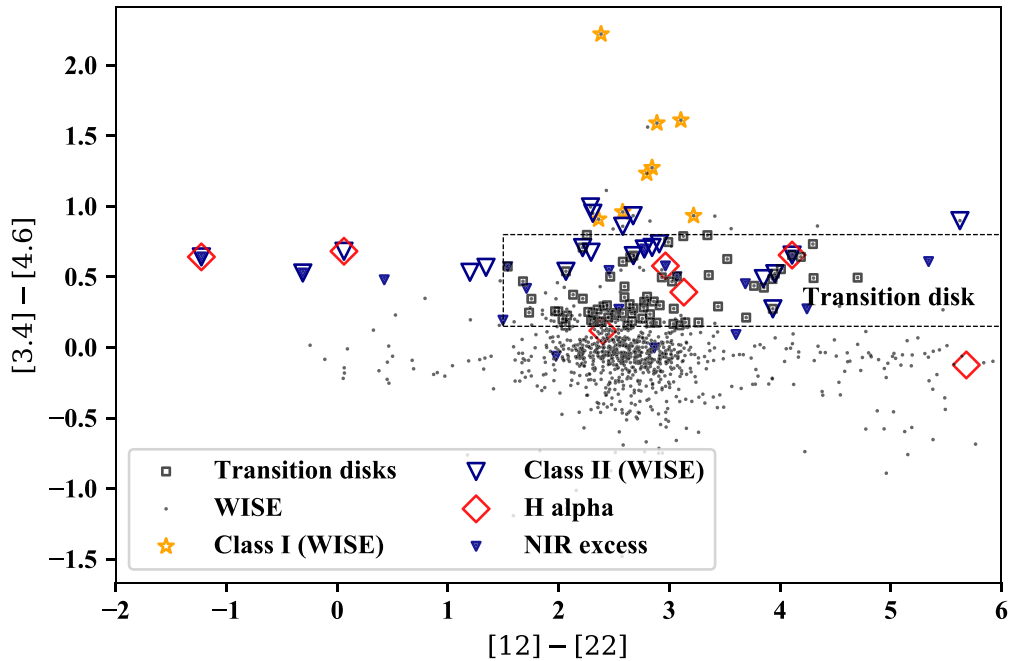


**Figure 4.** The WISE color-color diagram, similar to Figure 3 but here extends to 22  $\mu\text{m}$ , where transition disks are likely to be found, is marked in this figure. The Class I and Class II objects identified in Figure 3 are marked with the same symbols. Note that Class II objects do not stand out distinctly in this diagram. Black dots represent data points with a photometric error  $< 0.1$  mag in each of the four WISE bands.

### 3.1. Emission-line and Near-infrared Excess Stars

PMS stars are known to exhibit the  $\text{H}\alpha$  line emission in their spectra as a sign of chromospheric activity or circumstellar accretion, both indicative of stellar youth. We adopted the sample of 14  $\text{H}\alpha$  emission stars compiled by Ogura et al. (2002) that are mostly located outside or near the tip of BRC 43, as illustrated by the blue square in Figure 1 of the spatial coverage of our study. The equivalent width listed in their work allows distinction between classical T Tauri stars

(CTTS, with  $\text{EW} > 10 \text{ \AA}$ ) and weak-lined T Tauri stars (with  $\text{EW} < 10 \text{ \AA}$ ), the latter being relatively more evolved so as to have largely cleared their inner disks. This sample is limited in spatial coverage and, being detected in optical wavelengths, is also biased against embedded sources. Relatively evolved stars, such as magnetically active dwarfs (dMe) are potential contaminants.

Excess of infrared emission is the consequence of absorption of starlight in UV and visible by circumstellar grains, which

then reradiates at longer wavelengths. The position in a color-color diagram essentially represents different slopes in the spectral energy distributions (SEDs), with  $\alpha = d \log(\lambda F_\lambda) / d \log(\lambda)$ , where  $\lambda$  is the wavelength,  $F_\lambda$  is the flux density, and the slope  $\alpha$  serves as the proxy of the amount of thermalized dust, and hence the evolutionary stages of YSOs. Here we use a  $J - H$  versus  $H - K_s$  color-color diagram capable of qualifying the level of infrared excess and distinguishing this from interstellar reddening. Of the 18,316 2MASS sources in our field, 6901 have the photometric quality flag “AAA,” i.e., with an uncertainty less than 0.1 mag in all of the three bands. These are the stars used in our analysis for the 2MASS sample. Comparison of the observed 2MASS colors with the intrinsic loci of main-sequence stars and of giants, including added effects of interstellar reddening, leads to classification, in progressively increasing infrared excess (proxy of amounts of circumstellar dust), of classical T Tauri (solar-type) candidates, Herbig Ae/Be (intermediate-mass PMS) candidates, or proto-stars. In Figure 2, the rightmost trapezoid enclosing reddened T Tauri stars, but excluding main-sequence stars experiencing normal interstellar reddening, signifies the region within which young stars are likely located. A total of 29 such near-infrared excess objects, namely classical T Tauri candidates, were identified. These are shown in Figure 2, together with H $\alpha$  emission sources.

### 3.2. Mid-infrared Excess Stars

Deeply embedded stars may escape 2MASS detection; these are then selected from archival WISE data. Of the 9457 sources in the region, 1846 have photometric uncertainties less than 0.1 mag in 3.4  $\mu\text{m}$  (W1), 4.6  $\mu\text{m}$  (W2), and 12  $\mu\text{m}$  (W3), with the quality flag “AAA.” We adopted the scheme of Koenig & Leisawitz (2014), i.e., with color cuts from W1 to W3 for different YSO classes while winnowing out extragalactic contaminants such as active galactic nuclei or star-forming galaxies. Using (W1)–(W2) versus (W2)–(W3), we retrieved eight Class I and 21 Class II objects, as illustrated in Figure 3. Three out of eight Class I objects have reliable detection in every 2MASS band, each with the consistency of near-infrared excess. The remaining five do not have reliable 2MASS measurements, plausibly indicative of elevated extinction. Out of the 21 WISE-selected T Tauri candidates, 13 appear to also exhibit an excess of near-infrared ( $J - H \gtrsim 0.75$  and  $H - K_s \gtrsim 0.4$  in Figure 2). Four of the 21 WISE-selected T Tauri candidates are also common to the near-infrared-selected CTTS sample.

More embedded sources need to be investigated at longer wavelengths. Figure 4 presents the W1 – W2 versus W3 – W4 color-color diagram, in which transition disk objects stand out, exhibiting excess in 10–20  $\mu\text{m}$ . By contrast, Class II objects with prominent near-infrared excess can no longer be selected distinctly in this diagram as in Figure 2 or Figure 3. Note that in Figure 4, a few H $\alpha$  stars, candidate CTTSs are also common to transition disk objects, which are a subset of T Tauri stars with the inner disks being cleared; that is, they are in an evolutionary phase between Class II and Class III objects, and the common ones are included in our young stellar sample. The analysis above demonstrates the necessity of using a combination of colors, data quality permitting, with a wider range of wavelength coverage to acquire a more complete YSO sample. The catalog of PMS candidates is presented in the Appendix (Table 2).

We matched counterparts within a 3'' radius with the BVI (this work), 2MASS, and WISE sources to construct the SED of each

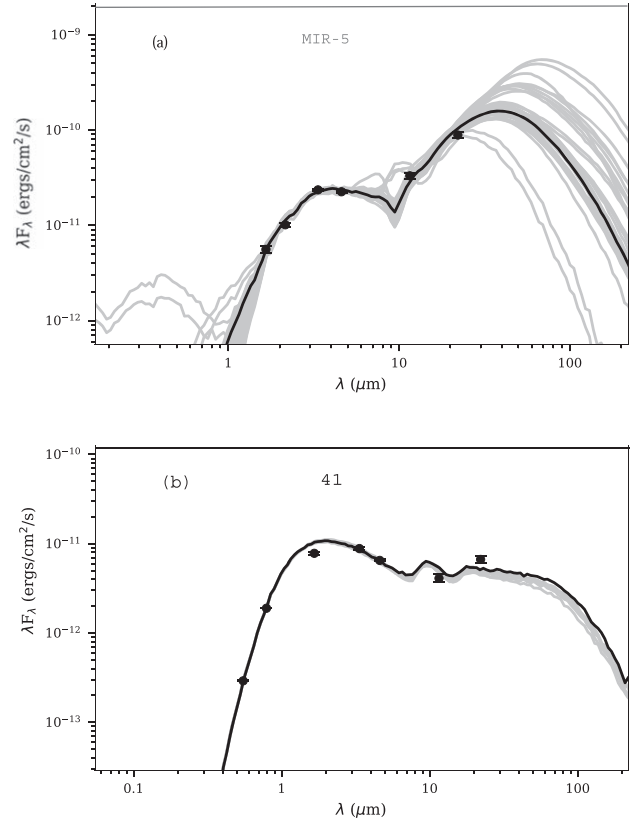


**Figure 5.** Example SEDs of (top) a Class I and (bottom) a Class II object. In each case, the source identification number is labeled. The black curve represents the best-fit model in the least-squares sense, and the gray curves indicate models with the range of reasonably good fits, i.e., with  $\chi^2_{\min} - \chi^2 < 3N$ , where  $N$  is the number of observational data points. The best-fit parameters of the Class I object, MIR-5, are listed in Table 1.

source for further investigation. The SED fitting was done with the tool developed by Robitaille et al. (2007), which uses a precomputed grid of 20,000 young stellar models to constrain the parameters for the central object (e.g., mass, temperature, age) and for the envelope (e.g., disk mass and accretion rate). The number of observational data points, and respective wavelength coverage, dictates the reliability of the constraints on the parameters. We required a minimum of four data points in an SED, and allowed in the fitting the extinction ( $A_V$ ) to vary from 1.5 mag (minimum foreground extinction toward the cluster) to 15 mag, and the distance to vary from 2.2 to 3.5 kpc, encompassing the literature values (Georgelin & Georgelin 1976; Moffat 1971; Chavarría-K et al. 1994). Figure 5 illustrates the distinct SED behavior of an example of a Class I with an ascending SED with wavelength versus that of a Class II object. The best-fit parameters such as the disk mass ( $M_{\text{Disk}}$ ), central object mass ( $M_*$ ), temperature ( $T_*$ ), adopting the approach given in Samal et al. (2012) using weighted mean and the standard deviation, are presented in Table 1 for Class I objects. The results suggest that most Class I objects have ages  $\lesssim 1$  Myr, consistent with them being young and embedded.

## 4. Properties of Young Stars

### 4.1. Kinematics of the Young Stellar Sample

We cross-matched the list of young objects in the region with Gaia EDR3 sources (Gaia Collaboration 2020) within a

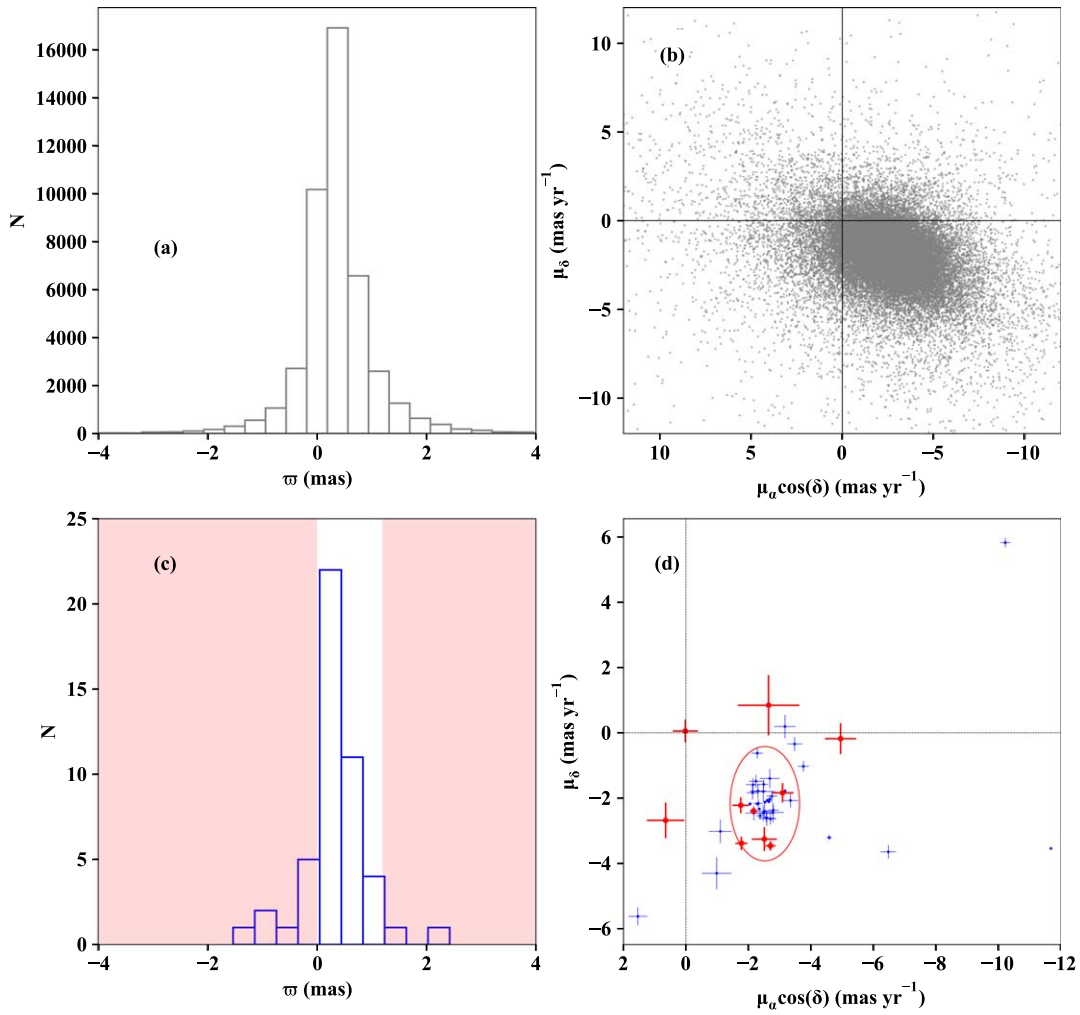


**Figure 6.** (a) Gaia EDR3 parallax and (b) proper motion vectors for all sources, whereas (c) and (d) show the same for the young stellar sample (in blue). In (d) the ellipse depicts 4 times median-absolute deviation of the young sample, centered on the mean proper motion for the cluster NGC 7380. Those stars in the shaded region in (c) having  $\varpi \leq 0$  or  $\varpi \geq 1.2$  mas, signifying uncertain parallax membership, are marked by red symbols in (d).

**Table 1**  
SED Fitting Parameters for Class I YSOs

ID	$\alpha$ (J2000) (deg)	$\delta$ (J2000) (deg)	[3.4] – [4.6] (mag)	[4.6] – [12] (mag)	Age (Myr)	$M_*$ ( $M_\odot$ )	$T_*$ ( $10^3$ K)	$M_{\text{Disk}}$ ( $M_\odot$ )	$\dot{M}$ ( $10^{-5} M_\odot \text{ yr}^{-1}$ )
MIR-1	341.440025	57.847372	1.590	3.475	0.002	0.623	3.776	0.006	17.637
MIR-2	341.575326	57.989582	1.611	3.221	0.937	0.850	4.842	0.006	10.649
MIR-3	341.642634	57.995816	1.234	3.549	0.021	2.455	4.09	0.033	466.956
MIR-4	341.943429	58.130137	1.274	3.859	0.015	4.73	4.224	0.036	67.637
MIR-5	341.969577	58.131370	0.934	3.256	0.713	3.26	5.864	0.063	16.305
MIR-6	341.981224	58.160661	2.221	4.099	2.470	3.661	12.547	0.025	92.607
MIR-7	341.898887	58.153404	0.960	3.331	0.500	4.891	7.9	0.000	50.080
MIR-8	341.93185	58.328075	0.909	3.153	0.258	0.343	2.961	0.004	0.786

coincidence radius of  $2''$ , resulting in two out of eight candidate protostars (Class I), and 46 out of 54 PMS objects having parallax and proper motion measurements. To our knowledge, no radial velocity information is available in the literature for any of the matched sources. The Gaia EDR3 ID and measurements are listed in the YSO catalog presented in the [Appendix](#). The distributions of parallax and proper motion values are shown in Figure 6. The region of our study is nebulous, rendering accurate astrometric estimation, with which parallax and proper motion are derived, difficult. This

is evident by a noticeable fraction of negative parallax values, including some of our young candidates. The median motion of the young stellar sample is  $(\mu_\alpha \cos \delta, \mu_\delta) = (-2.52, -2.16)$   $\text{mas yr}^{-1}$  which is also close to the average proper motions of the cluster NGC 7380,  $(\mu_\alpha \cos \delta, \mu_\delta) = (-2.517 \pm 0.131, -2.144 \pm 0.131)$   $\text{mas yr}^{-1}$  (Cantat-Gaudin et al. 2018). Those objects that deviate more than 4 times the median absolute deviation, therefore being inconsistent with the cluster’s motion, are noted in Figure 6(d) and in Table 2 in the [Appendix](#). In Figure 6(c) those young stars having  $\varpi \leq 0$  or

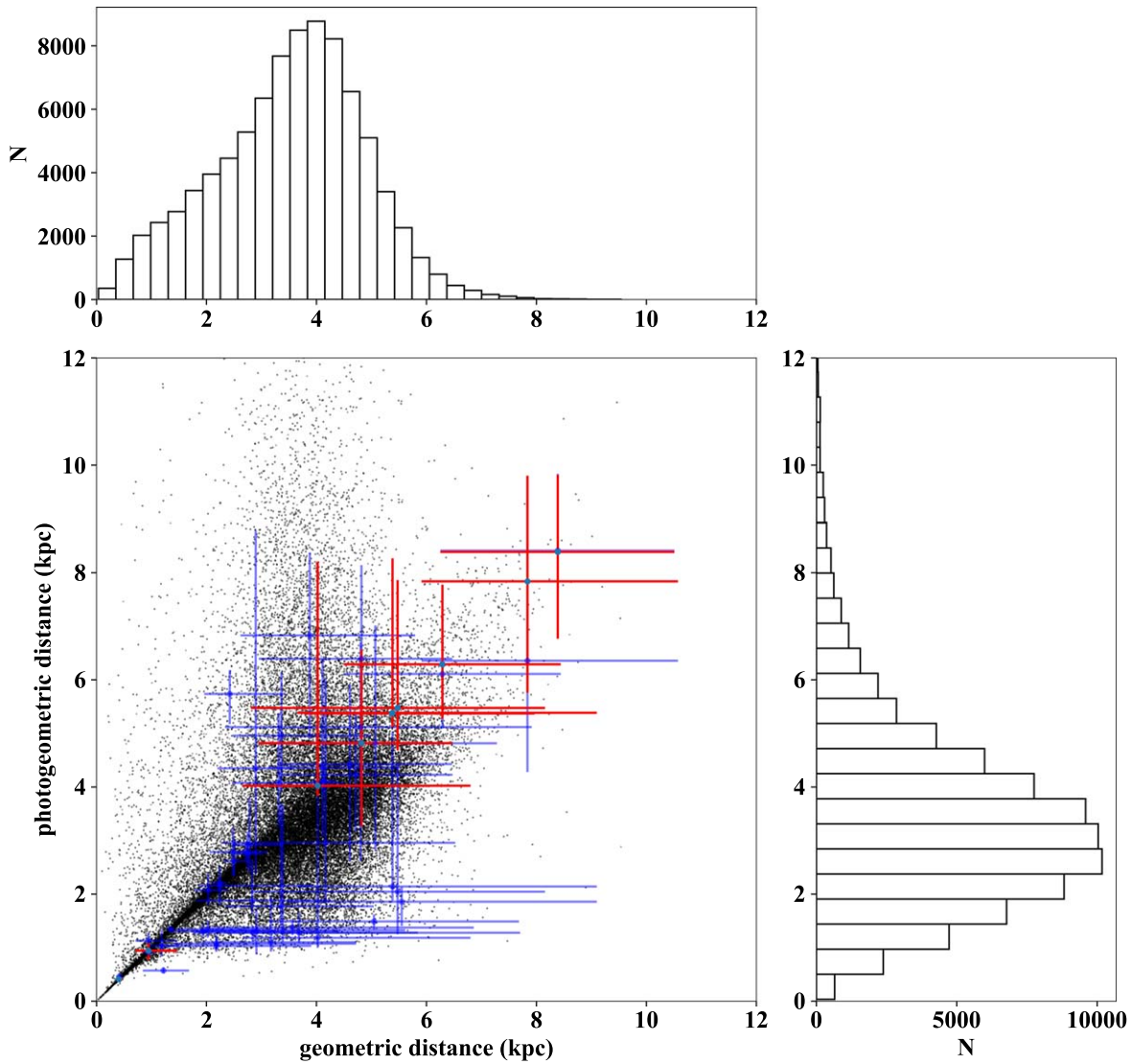


**Figure 7.** Geometric vs. photogeometric distance estimated by Bailer-Jones et al. (2021), and the respective number distribution. The black points represent all sources, whereas the blue symbols mark the YSO sample along with asymmetric error bars. The red symbols show the YSOs as parallax outliers in the shaded region in Figure 6(c), also the red crosses in Figure 6(d).

$\varpi \geq 1.2$  mas, which would have been excluded of membership however exhibit a grouping in proper motion (Figure 6(d)) consistent with that of the cluster NGC 7380.

There are objects with large deviations from the cluster’s average proper motion, yet with youth indicators such as  $H\alpha$  or infrared excess. For example, Star 34, a near-infrared candidate exhibiting outlying proper motion of  $(-10.2, 5.8)$  mas yr $^{-1}$ , a parallax of  $1.06 \pm 0.14$  mas, and a distance of  $0.94^{+0.13}_{-0.11}$  kpc, is likely not a member. Other examples include the  $H\alpha$  star 9, and the candidate young star 37, both having motions inconsistent with membership. Four objects, namely stars 6, 23, 26, and 43, have negative parallax values and their proper motions are also not in accord with membership.

To remedy the effects of negative parallax, Bailer-Jones et al. (2021) derived the Bayesian geometric distances by direction-dependent prior from a parallax value and its uncertainties. Additionally these authors also estimate a photogeometric distance based on the color, apparent magnitude, and extinction of a source. We compare the distributions of both distance determinations, shown in Figure 7, for all Gaia sources and for the YSO sample in our field of study. It is

evident that the errors in distance computation for the YSOs are substantially large, essentially for those with negative parallax values.

Notably, Star 11<sup>6</sup> is plausibly one of the stars whose parallax data are affected by the copious H II nebulosity. As remarked in Table 2, it is a known emission-line object (Ogura et al. 2002) and exhibits prominent infrared excess. Its parallax  $2.42 \pm 0.26$  mas, however, would place it at a heliocentric distance of  $\sim 413$  pc and a geometric distance of  $409.1^{+73.7}_{-40.7}$  pc, making it a puzzling, isolated, foreground young star. Nevertheless, its proper motion remains consistent with being a member of the cluster. The above analysis thus indicates the primacy of proper motions over parallaxes in establishing the association of young objects to Sh 2-142.

#### 4.2. Interconnection between Young Stars and Gas

Our CO data presented in Figures 8 and 9 evince spatial and kinematic structures of the molecular gas in the region.

<sup>6</sup> Gaia EDR3 ID 2007420160273312512.

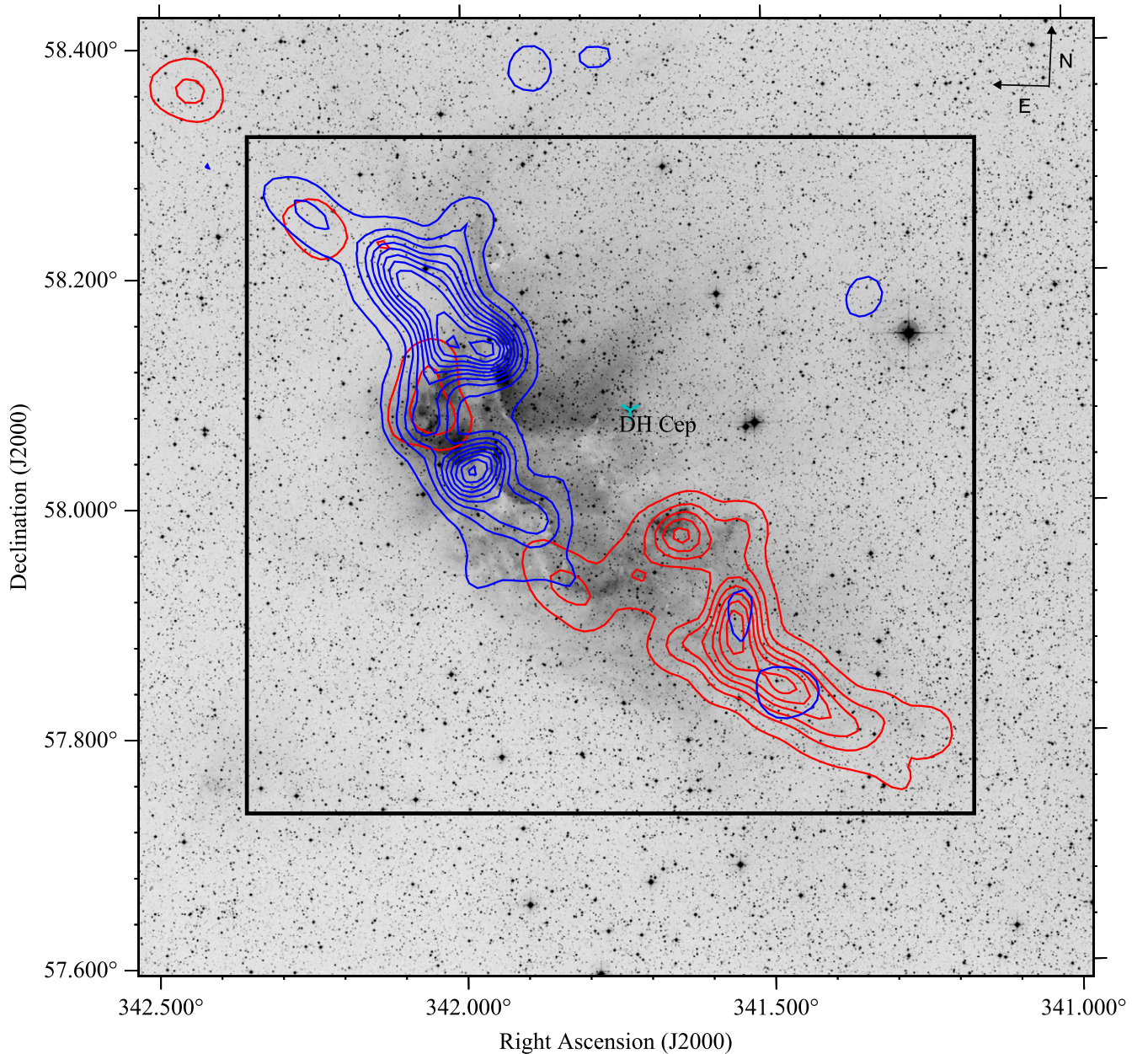


**Figure 8.** Integrated  $^{12}\text{CO}$  emission contours overlaid on the DSS2 red image, of the velocity range from  $-45$  to  $-39$   $\text{km s}^{-1}$  (in blue), and from  $-39$  to  $-35$   $\text{km s}^{-1}$  (in red). Contours are plotted from the minimum of  $3\sigma$ , in steps of  $3.5$   $\text{K km s}^{-1}$ . The southwest lobe is redshifted relative to the northeast lobe. The black square marks the boundary for which the integrated CO spectrum is shown in the subsequent Figure 9.

Spatially averaged and summed spectra, for  $^{12}\text{CO}$  and isotopic  $^{13}\text{CO}$  lines, clearly indicate two main lobes in the velocity range of  $-55$  to  $-25$   $\text{km s}^{-1}$ , bifurcating around  $-39$   $\text{km s}^{-1}$ . The  $^{13}\text{CO}$  lines are weaker, but consistently validate the kinematic and spatial segregation of the gas. The  $\text{C}^{18}\text{O}$  emission is much weaker, hence not considered in our analysis.

The radial velocity of DH Cep,  $-35.4 \pm 2.0$   $\text{km s}^{-1}$  (Wilson 1953), matches that of the average value of NGC 7380,  $-34.13 \pm 6.09$   $\text{km s}^{-1}$  (Kharchenko et al. 2005; Conrad et al. 2017). Jointly these then agree with the line-of-sight velocity of the bulk molecular gas, thus establishing the physical connection of the gas, star cluster, and the main exciting star in the complex.

Morphologically, the CO emission clearly embraces the cluster (Leisawitz et al. 1989; Chen et al. 2011), with a northeast–southwest extension, mainly in the two lobes

comparable in spatial extents but distinguished in kinematics. The two velocity peaks are  $\sim 4$   $\text{km s}^{-1}$  apart, with each peak corresponding to a lobe, in agreement with what has been reported by Joncas et al. (1988). Similarity in peak velocities of the two lobes with distinctive space volumes suggests that the clouds are not independent. Slicing through the channel maps with a step of  $1$   $\text{km s}^{-1}$  reveals no systematic trend indicative of an overall cloud rotation. On the other hand, the lobes are projected to have a separation of  $\sim 25$  pc at  $2.6$  kpc, a length scale too long for a protostellar outflow. Typical length scales for molecular outflows are of the order of a parsec (Levreault 1988). The two lobes therefore cannot be due to either cloud rotation or stellar outflows.

The relative symmetry of the lobes, plus the small velocity gradient across the cloud, indicates that the lobes are near the plane of the sky. We propose that the two lobes are parts of the

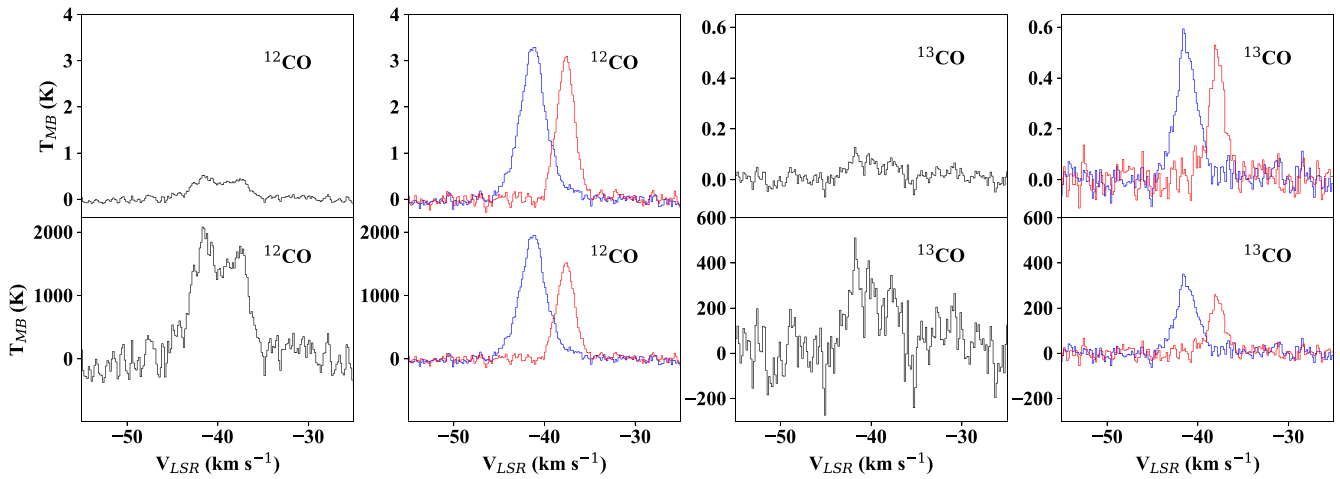


**Figure 9.** The average (upper panels) and summed (lower panels) spectra between  $-55$  and  $-25$   $\text{km s}^{-1}$  for the  $^{12}\text{CO}$  and  $^{13}\text{CO}$  lines. Each black curve shows the corresponding spectra within the black square area in Figure 8. The red and blue curves trace the outermost  $3\sigma$  contour for, respectively, the blue- and redshifted lobes outlined in Figure 8.

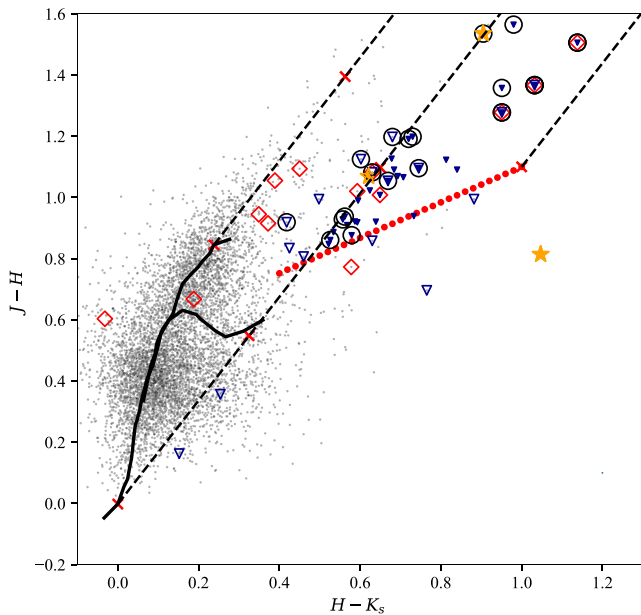


**Figure 10.**  $JHK$  color-color diagram for the  $H\alpha$  stars (in red diamonds), and near-infrared stars (in filled blue triangles). Also shown are 2MASS counterparts of some of the Class I (orange asterisks) and Class II (open blue triangles) sources identified with the WISE data (see Figure 3).

“working surface” of the stellar winds and ionizing shock fronts upon the compressed clouds. There are a couple of known O-type stars in the region (Chen et al. 2011), notably the DH Cep binary system, which emits copious X-rays possibly due to powerful colliding winds (Pittard & Stevens 2002; Bhatt et al. 2010). Such a phenomenon is seen also, for example, in Orion and Monoceros where massive stars, molecular gas, and photoionized gas interplay.

#### 4.3. Reddening and Ages

Of the  $H\alpha$  stars (14), near-infrared (29), and mid-infrared excess (29) objects, 38/62 are consistent with being classical T Tauri stars in the NIR color-color diagram (see Figure 10). A few objects displaying less infrared excess yet with  $H\alpha$  emission are likely evolved PMS, namely weak-lined T Tauri

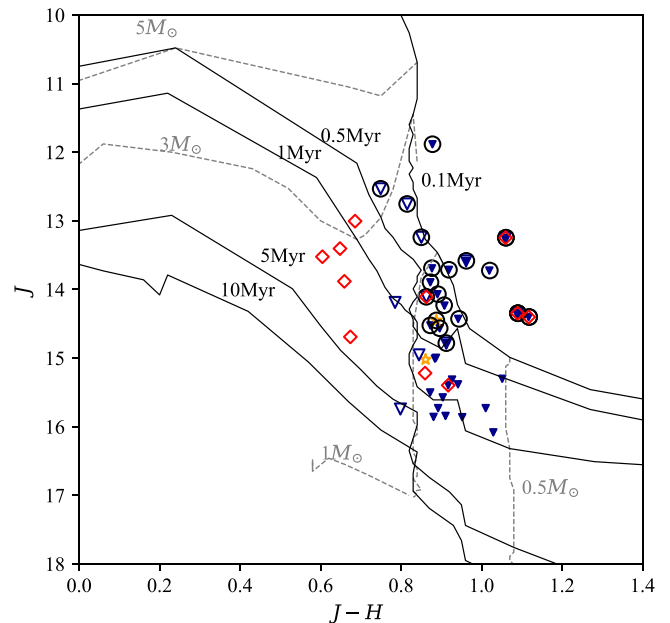


**Figure 11.** Dereddened 2MASS  $J$  vs.  $J-H$  color-magnitude diagram for the young stars, with the same symbols as in Figure 10, in comparison with PMS theoretical isochrones, and evolutionary tracks of Siess et al. (2000), corrected for a distance of 2.6 kpc, with the ages (solid curves) and masses (dashed curves) marked and labeled. The observed  $J$  and  $J-H$  values are extinction corrected and dereddened according to the reddening law from Cohen et al. (1981). The youngest objects are encircled in black.

stars. To estimate the extinction of each star, we tracked back in the diagram along the reddening vector from the observed colors to the intrinsic classical T Tauri locus (the red line) or, for those outside the T Tauri regime, to the main sequence (the black curve). This analysis obviously does not apply to heavily embedded objects as they are not detected by 2MASS.

Once the extinction is estimated, a young object is dereddened and placed in a color-magnitude diagram to infer its age and mass by comparison with theoretical isochrones, e.g., in the  $J$  versus  $J-H$  diagram as exhibited in Figure 11. While isochrone ages may not be reliable in an absolute sense, it is seen that a few  $H\alpha$  stars are relatively older than the near-infrared excess sources. Most of the young population have

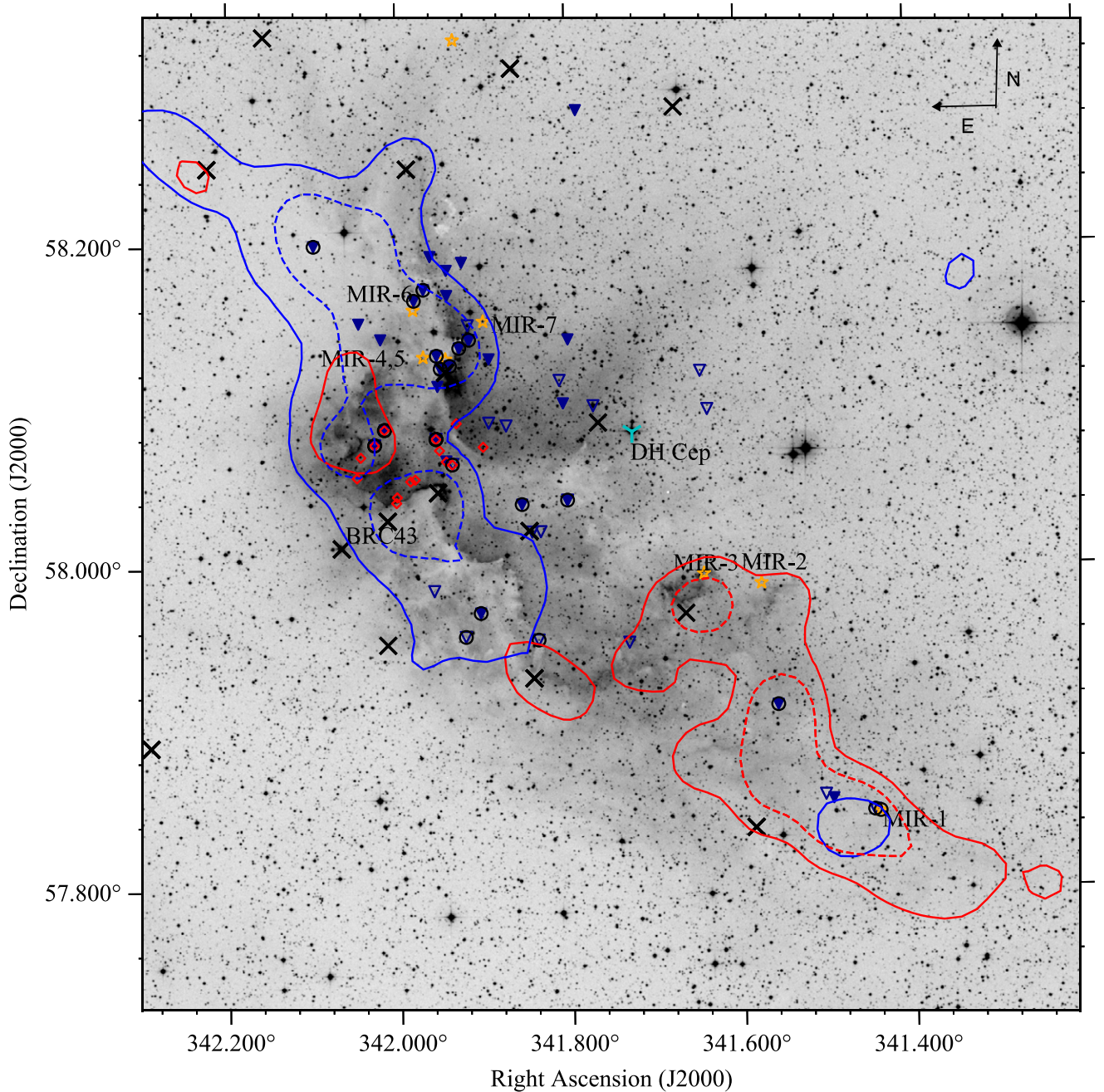


**Figure 12.** Location of all the young stellar objects, with the symbols the same as in Figure 10, on a DSS2 red image, together with IRAS point sources (Helou & Walker 1988) as protostar candidates (black crosses). The Class I (MIR) sources and DH Cep are labeled. Overlaid are contours for emission from  $^{12}\text{CO}$  (solid contours) and  $^{13}\text{CO}$  (dashed contours) integrated into the velocity range of  $-45$  to  $-39$   $\text{km s}^{-1}$  in blue, and  $-39$  to  $-35$   $\text{km s}^{-1}$  in red. For clarity, only the outermost contours are shown at  $5\sigma$  level, with  $\sigma$  being the sky background, to trace the cloud perimeter.

masses  $\lesssim 1 M_{\odot}$ . The objects comprising the youngest group, with isochrone ages  $\lesssim 0.5$  Myr, are marked separately for further scrutiny.

#### 4.4. Spatial Distribution

With the list of the young population at different evolutionary stages, we are ready to delineate their relative locations with respect to parental/remnant gas. Figure 12 displays their positions, now including also those of IRAS point sources as potential protostars. The young stars are numerous in the northeastern part of the cloud and are

concentrated around BRC43. To the northeast, where the molecular gas interacts with the ionization front, there are one IRAS source and three Class I (MIR-4, MIR-5, and MIR-6) sources, together with a young group of PMS objects associated with the cloud, some located near the rim. Outside the cloud, there is only one Class I source (MIR-7), and there are several T Tauri stars, all aligned in the direction of DH Cep. This MIR-7 source, earlier considered as a field variable star (Lata et al. 2016), in fact exhibits a Class I SED and has proper motion  $(-2.53, -2.12)$   $\text{mas yr}^{-1}$  and parallax  $0.37 \pm 0.04$  mas (Gaia Collaboration 2020), consistent with being a member of NGC 7380, which has an average proper motion of  $(-2.51,$

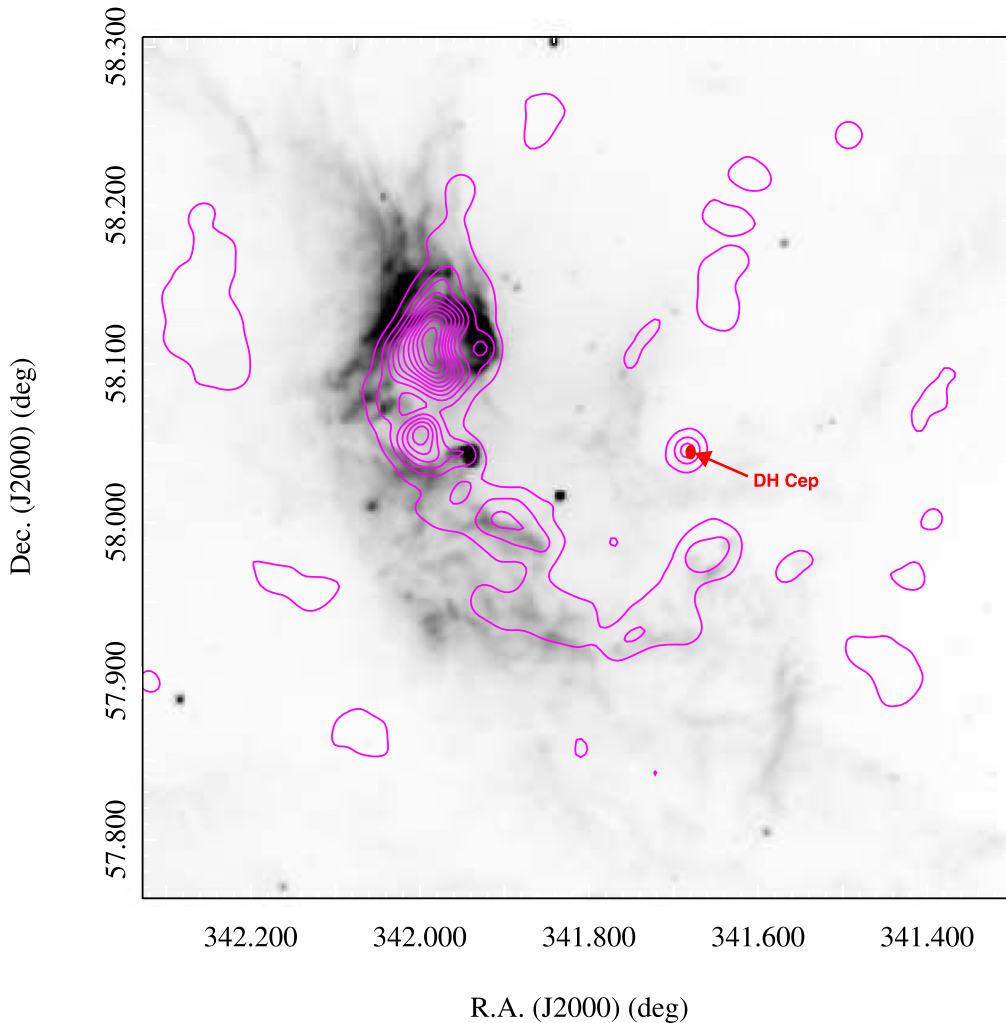


**Figure 13.** The NVSS 1.4 GHz continuum emission (contours in magenta) tracing hot plasma overlaid on the WISE 12  $\mu\text{m}$  image (in grayscale). The lowest contour level is at  $3\sigma$ , with  $\sigma$  being  $0.0005 \text{ Jy beam}^{-1}$ , with increments of  $0.004 \text{ Jy beam}^{-1}$ .

$-2.14) \text{ mas yr}^{-1}$  and a parallax of  $0.33 \pm 0.05 \text{ mas}$  (Cantat-Gaudin et al. 2018).

In the BRC 43 extension, five out of 14  $\text{H}\alpha$  objects (limited to this region) are common to the classical T Tauri stars in our sample, whereas the remaining  $\text{H}\alpha$  objects are possibly weak-lined T Tauri stars. All these line up roughly toward DH Cep as well. Our analysis of the infrared data shows no Class I or Class II objects inside BRC 43, except a previously known IRAS point source (Sugitani et al. 1991) and a submillimeter source (Morgan et al. 2008). As in the northeast extension, here the youngest objects, those encircled in Figure 11, seem preferentially associated with dense parts of the cloud.

In addition to these two extensions, there are less prominent concentrations revealed by the CO data, notably the one in the southwest that harbors an IRAS source and with MIR-2 and MIR-3 located near its periphery, tantalizingly enough, facing DH Cep. The southernmost reach of the complex, distant from the massive stars and from ionized gas, still shows the presence of a few PMS objects and a protostar (MIR-1). Unlike the northeastern lobe where young stars are present inside and outside of the remnant molecular clouds that must have been carved out, here there is a paucity of relatively evolved young stars, and existing young stars have all been formed in situ within the comparatively unperturbed cloud.

## 5. Discussion

The region of our study, comprising a full-fledged star cluster, highly luminous stars photoionizing surrounding gas, and molecular cloud complex that must have partly given birth to these stars, yet partly survived the fierce environments to sustain present-day star formation, provides a plausible scenario of stellar feedback. The relational sequence in position and age of next-generation young stars with respect to the parental clouds along with their manifestations as individual globules, or bright-rimmed clouds, and to the massive stars serve as vital tools to identify prompted star formation. Such configuration is amply exhibited, e.g., in the Orion clouds (Sugitani et al. 1989; Ramesh 1995; Lee et al. 2005; Gandolfi et al. 2008; Cernicharo et al. 1992).

Our analysis indicates that most Class I and IRAS objects, signposts of ongoing star formation, are embedded and located near rims. Moreover, the young stars line up roughly perpendicular to the rims, with bluer (presumably older) stars closer to, thereby exposing a star birth sequence is therefore shown to start (Sugitani et al. 1995; Ogura et al. 2002; Lee et al. 2005; Ogura et al. 2007; Chauhan et al. 2009). In addition to the distribution of molecular material, Figure 13 presents the associated ionized gas distinctly compressed in the northeastern extension, through BRC 43, and stretching further to the upper

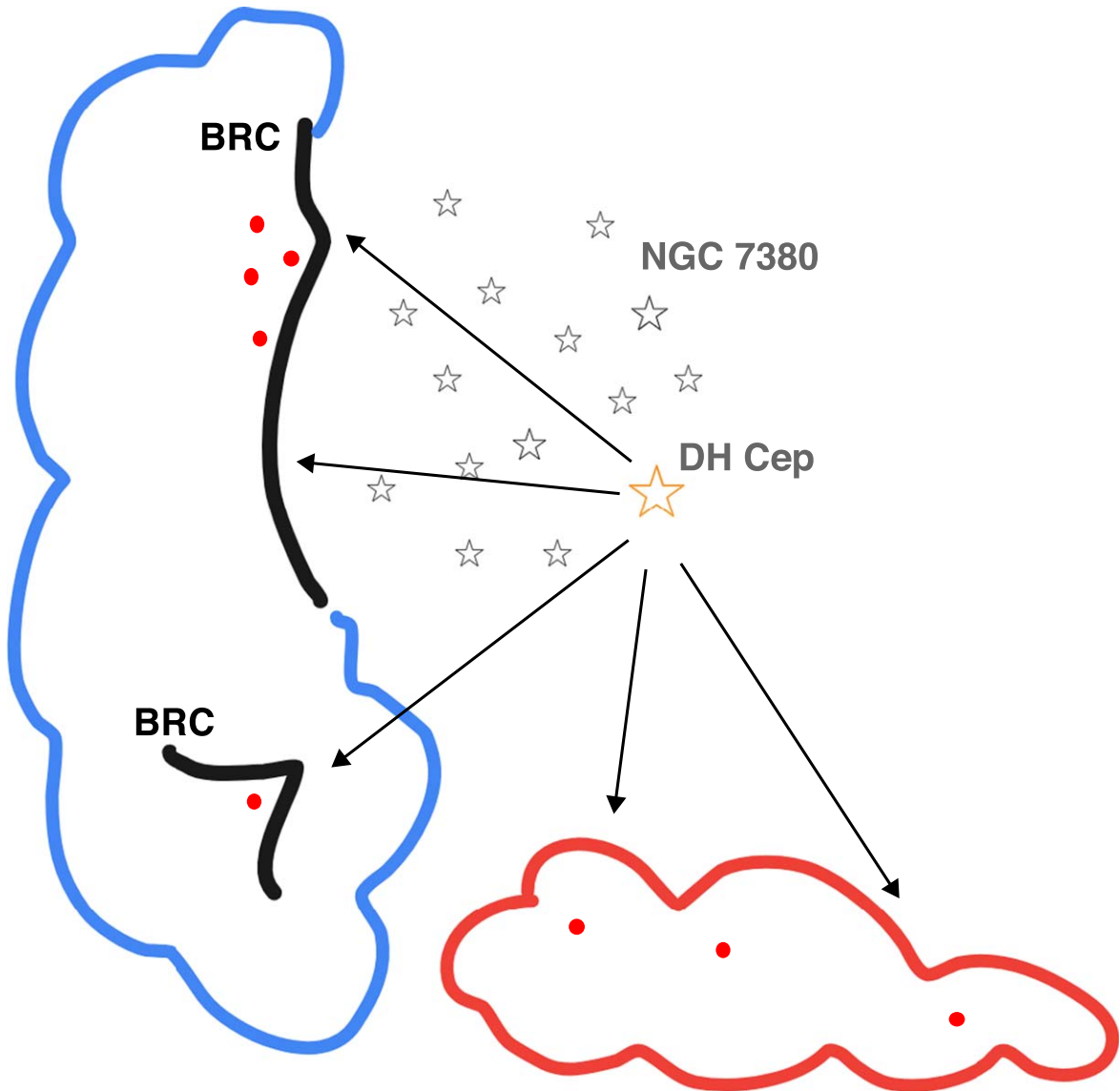


**Figure 14.** The schematic (not to scale) for the Sh 2-142 region. The asterisks represent the open cluster NGC 7380, the orange asterisk the major exciting star DH Cep. Bright-rimmed clouds are marked, along with the red- and blueshifted lobes of the molecular gas. The red dots show the youngest objects ( $\lesssim 1$  Myr). The arrows emanating from DH Cep show possible propagation directions of ionizing fronts.

southwestern lobe. This is in support of an expanding ionization front originated from DH Cep.

The feasibility of a triggering scenario must be substantiated by reasonable timescales (Karr & Martin 2003; Lee et al. 2005). To consider an extant OB star still in existence as the external trigger, its age must be greater or comparable to the propagation time of the ionization front through the cloud, plus the age of the young population. In our case, the expected main-sequence lifetime of DH Cep is  $\sim 1.5$  Myr (Hilditch et al. 1996), and given a projected distance of 5.6 pc between BRC 43 and DH Cep, the propagation time for the perturbing front, assuming a typical sound speed of  $10 \text{ km s}^{-1}$ , is  $\sim 0.5$  Myr. The northeastern extension is physically closer to, and hence reasonably coeval with, NGC 7380. Since the youngest population is  $\lesssim 1$  Myr old, these timescales are consistent with a sequential star formation in the region. Figure 14 presents the schematic of the cloud complex comprising its main components namely, cluster, DH Cep,

BRCs along with relatively young population associated with the cloud, to sum up our findings and inference.

There are limits and uncertainties of our interpretation. Massive stars do not always play a constructive role to clouds that otherwise would not collapse spontaneously, as is the case proposed in this work. For example, they could disrupt a cloud so as to quench any consequent formation possibilities. On the stellar scales, a young stellar disk/envelope can be photo-evaporated by scorching radiation from nearby massive stars (Beltrán et al. 2009), or swept by their winds, disguising a bona fide infant object as being devoid of circumstellar matter, hence seemingly evolved. This will affect the level of infrared excess as the amount of circumstellar dust which is a key indicator of the youth of an object and its evolutionary stage. Therefore the age argument plus the nonrandom spatial distribution of the young population presented here lends support to the decisive influence of massive stars on environments in the case of prompted star formation.

TS and WPC acknowledge the financial support of this work by the MoST grant 109-2112-M-008-015-MY3. This research made use of the data from the Milky Way Imaging Scroll Painting (MWISP) project, which is a multiline survey in  $^{12}\text{CO}/^{13}\text{CO}/\text{C}^{18}\text{O}$  along the northern galactic plane with PMO-13.7 m telescope. We are grateful to all the members of the MWISP working group, particularly the staff members at PMO-13.7 m telescope for their long-term support. MWISP was sponsored by the National Key R&D Program of China with grant 2017YFA0402701 and CAS Key Research Program of Frontier Sciences with grant QYZDJ-SSW-SLH047. YS is supported by the National Natural Science Foundation of China through grant 11773077 and the Youth Innovation Promotion Association, CAS (2018355). Y.G. acknowledges support by the National Key Basic R&D Program of China (2017YFA0402704), NSFC grant 11861131007, 12033004. This publication makes use of data products from the Two Micron All Sky Survey, which is a joint project of the University of Massachusetts and the Infrared Processing and Analysis Center/California Institute of Technology, funded by the National Aeronautics and Space Administration and the National Science Foundation. This publication makes use of

data products from the Wide-field Infrared Survey Explorer, which is a joint project of the University of California, Los Angeles, and the Jet Propulsion Laboratory/California Institute of Technology, funded by the National Aeronautics and Space Administration. This work has made use of data from the European Space Agency (ESA) mission Gaia (<https://www.cosmos.esa.int/gaia>), processed by the Gaia Data Processing and Analysis Consortium (DPAC, <https://www.cosmos.esa.int/web/gaia/dpac/consortium>). Funding for the DPAC has been provided by national institutions, in particular the institutions participating in the Gaia Multilateral Agreement. This research has made use of the services of the ESO Science Archive Facility.

### **Appendix Catalog of Young Stars**

In addition to the Class I objects listed in Table 1, we present in Table 2 other classes of young stars, including  $\text{H}\alpha$  emission stars, near-infrared and mid-infrared excess stars identified from the 2MASS and WISE data respectively. Table 2 lists the  $V$  magnitude,  $J - H$  and  $H - K_s$  colors, WISE colors, and Gaia EDR3 measurements.

**Table 2**  
List of Young Stars in Sh 2-142

ID	$\alpha$ (J2000) (deg)	$\delta$ (J2000) (deg)	Gaia ID	$V$ (mag)	$J - H$ (mag)	$H - K_s$ (mag)	[3.4] - [4.6]	[12] - [22]	$\mu_\alpha \cos \delta$ (mas yr $^{-1}$ )	$\mu_\delta$ (mas yr $^{-1}$ )	Remarks <sup>a</sup>	
1	341.900000	58.075556	2007418893273376384	16.777 (0.004)	0.679	0.222	-0.124	0.275	0.1852 (0.1894)	-2.1311 (0.192)	-1.835 (0.204)	H $\alpha$
2	341.931250	58.090278	2007418996344878080	19.110 (0.011)	0.948	0.406	...	...	-0.3401 (0.1100)	-2.1633 (0.116)	-2.396 (0.109)	H $\alpha$ , <sup>b</sup>
3	341.936250	58.064722	2007418717164267776	19.414 (0.012)	1.129	0.664	0.682	2.421	0.3485 (0.1293)	-2.4842 (0.139)	-1.578 (0.141)	H $\alpha$
4	341.943333	58.066667	2007418717170804224	20.997 (0.057)	1.049	0.683	...	...	0.6829 (0.2371)	-2.5157 (0.258)	-2.399 (0.243)	H $\alpha$
5	341.951250	58.073611	2007418927625454208	20.188 (0.023)	1.142	0.484	...	...	0.2012 (0.1973)	-2.2366 (0.216)	-1.482 (0.198)	H $\alpha$ , NIR
6	341.955417	58.080556	2007418927633127936	21.129 (0.055)	1.439	1.066	0.655	2.718	-1.5337 (0.5589)	0.6507 (0.600)	-2.681 (0.547)	H $\alpha$ , NIR, TD, <sup>b,c</sup>
7	341.980000	58.055556	...	19.878 (0.017)	...	...	...	...	...	...	...	H $\alpha$
8	341.985417	58.054444	2007371747402090752	19.855 (0.018)	1.062	0.627	...	...	0.4861 (0.2089)	-2.1438 (0.225)	-1.588 (0.202)	H $\alpha$
9	342.001250	58.044722	2007371682977631744	18.837 (0.008)	1.100	0.423	0.392	1.700	0.3197 (0.2832)	1.5372 (0.293)	-5.622 (0.270)	H $\alpha$ , <sup>c</sup>
10	342.002083	58.041111	2007371678682606208	21.016 (0.044)	0.793	0.612	...	...	-0.5921 (0.3748)	-2.5072 (0.397)	-3.253 (0.362)	H $\alpha$ , <sup>b</sup>
11	342.015833	58.086389	2007420160273312512	20.129 (0.020)	1.590	1.172	0.578	1.475	2.4237 (0.2641)	-1.7524 (0.267)	-2.218 (0.245)	H $\alpha$ , NIR, <sup>b</sup>
12	342.027500	58.076944	2007373263538670976	18.389 (0.006)	1.342	0.985	0.642	2.868	0.3252 (0.0563)	-2.0504 (0.058)	-2.175 (0.057)	H $\alpha$ , NIR, MIR
13	342.043750	58.069444	2007373194819202944	17.635 (0.005)	0.980	0.383	0.119	2.791	0.3701 (0.3625)	-1.0993 (0.365)	-3.017 (0.361)	H $\alpha$ , <sup>c</sup>
14	342.048333	58.056667	2007372984352672896	18.228 (0.007)	0.609	0.002	...	...	0.4374 (0.0824)	-4.5821 (0.086)	-3.206 (0.079)	H $\alpha$ , <sup>c</sup>
15	341.494397	57.855476	2007409783635818240	...	0.952	0.627	0.271	3.879	0.2884 (0.1585)	-2.7482 (0.170)	-1.939 (0.156)	NIR
16	341.557581	57.914074	2007410230308741376	...	0.962	0.591	0.452	2.100	0.3885 (0.0820)	-2.6836 (0.089)	-2.028 (0.087)	NIR
17	341.904388	57.972439	2007370854050001664	...	1.139	0.718	0.546	2.275	0.0417 (0.2449)	-2.5860 (0.269)	-2.610 (0.242)	NIR
18	341.801554	58.042183	2007419099424074752	...	1.099	0.703	0.698	2.815	0.8689 (0.4292)	-0.9822 (0.469)	-4.302 (0.490)	NIR, MIR, <sup>c</sup>
19	341.854893	58.039734	2007418412237051008	18.427 (0.009)	1.029	0.629	0.419	1.548	1.1627 (0.3412)	-3.1667 (0.346)	0.193 (0.355)	NIR, <sup>c</sup>
20	341.805658	58.102238	2007422496742049664	...	1.116	0.727	0.609	1.433	1.3603 (0.3307)	-3.0904 (0.349)	-1.835 (0.297)	NIR, <sup>b</sup>
21	341.949521	58.124252	2007419855346026752	16.328 (0.003)	0.889	0.560	0.503	4.240	0.3309 (0.0247)	-2.3453 (0.026)	-2.334 (0.025)	NIR, TD
22	341.953041	58.113277	2007419782322726912	...	1.178	0.712	...	...	0.4052 (0.3351)	-2.4728 (0.386)	-1.795 (0.323)	NIR
23	341.799320	58.141865	2007422879004712960	...	0.917	0.568	...	...	-0.7669 (0.8914)	-2.6417 (0.980)	0.845 (0.923)	NIR, <sup>b,c</sup>
24	341.915786	58.142029	2007420095864167552	17.847 (0.006)	1.144	0.779	0.528	1.973	0.4839 (0.0732)	-2.6501 (0.089)	-2.103 (0.068)	NIR, MIR
25	341.927422	58.136948	...	...	1.256	0.764	...	...	...	...	...	NIR
26	341.892512	58.130032	2007419992777147648	20.216 (0.034)	0.954	0.673	...	...	-0.1131 (0.4632)	-4.9446 (0.499)	-0.178 (0.469)	NIR, <sup>a,b</sup>
27	341.968923	58.173332	2007424562622310400	...	1.248	0.754	-0.062	2.459	0.6113 (0.2318)	-2.1720 (0.267)	-2.457 (0.223)	NIR
28	341.953892	58.132324	...	...	1.654	1.014	...	...	...	...	...	NIR
29	341.941872	58.185230	2007424627039547904	...	0.955	0.621	0.480	3.446	0.0829 (0.3162)	-2.7824 (0.346)	-2.440 (0.306)	NIR
30	341.938608	58.125923	2007419851042201600	...	1.429	0.985	0.574	4.879	0.3389 (0.2389)	-2.4699 (0.277)	-2.460 (0.243)	NIR, TD
31	341.941590	58.169617	2007423080851313664	...	1.065	0.658	0.092	-0.296	0.1464 (0.1478)	-2.7917 (0.174)	-2.365 (0.154)	NIR
32	341.980183	58.166515	2007421642052396672	17.222 (0.011)	0.906	0.613	...	...	0.3380 (0.0480)	-2.2764 (0.051)	-2.175 (0.045)	NIR
33	342.019767	58.142502	2007421294154343296	19.486 (0.014)	0.974	0.767	...	...	0.6906 (0.1668)	-3.7559 (0.179)	-1.024 (0.160)	NIR, <sup>c</sup>
34	342.045459	58.152340	2007421397224336000	...	1.139	0.874	...	...	1.0695 (0.1405)	-10.2152 (0.159)	5.828 (0.138)	NIR, <sup>c</sup>
35	341.923714	58.190090	2007423355735513472	...	0.942	0.602	...	...	0.5070 (0.2245)	-3.3429 (0.253)	-2.072 (0.220)	NIR
36	341.960885	58.193882	2007424631341712512	...	1.174	0.847	...	...	0.5393 (0.2330)	-2.3024 (0.268)	-1.781 (0.224)	NIR
37	342.097888	58.200584	2007422123088832000	16.610 (0.012)	0.972	0.596	-0.003	3.270	0.7183 (0.0377)	-11.6709 (0.041)	-3.541 (0.037)	NIR, <sup>c</sup>
38	341.787287	58.284023	2007437305785335168	...	0.875	0.556	0.274	0.767	0.4866 (0.1866)	-2.7023 (0.187)	-2.635 (0.170)	NIR
39	342.113152	58.353428	...	...	1.112	0.741	0.194	2.655	...	...	...	NIR
40	341.922024	57.957687	2007370102442790400	...	1.255	0.714	0.934	2.761	0.1644 (0.1255)	-2.5693 (0.132)	-2.603 (0.129)	MIR
41	341.958527	57.986312	2007370510452682624	19.571 (0.013)	1.124	0.812	0.651	2.340	0.4515 (0.1123)	-2.3725 (0.121)	-2.539 (0.117)	MIR, TD
42	341.836899	57.955555	2007370785329140480	...	1.176	0.636	0.540	2.083	0.1698 (0.1653)	-2.2811 (0.179)	-0.623 (0.164)	MIR
43	342.480315	58.197335	2007398444923197184	...	0.498	0.796	0.859	2.815	-0.2364 (0.3566)	0.0199 (0.403)	0.056 (0.342)	MIR, <sup>b,c</sup>
44	341.446427	57.848265	2007409616143542144	...	0.952	0.452	0.951	2.444	-0.0550 (0.1448)	-2.7023 (0.158)	-3.459 (0.145)	MIR, <sup>b</sup>
45	341.843310	58.022632	2007418171718891904	14.878 (0.007)	1.034	0.916	0.996	2.446	-0.8131 (0.1905)	-1.7739 (0.191)	-3.383 (0.207)	MIR, <sup>b</sup>
46	341.833242	58.022783	...	...	...	...	0.899	2.843	...	...	...	MIR
47	341.770388	58.100528	2007422462376242816	...	0.130	0.186	0.523	2.490	0.9336 (0.1975)	-3.4756 (0.236)	-0.342 (0.210)	MIR, TD, <sup>c</sup>

**Table 2**  
(Continued)

ID	$\alpha$ (J2000) (deg)	$\delta$ (J2000) (deg)	Gaia ID	$V$ (mag)	$J - H$ (mag)	$H - K_s$ (mag)	[3.4] - [4.6]	[12] - [22]	$\mu_\alpha \cos \delta$ (mas yr <sup>-1</sup> )	$\mu_\delta$ (mas yr <sup>-1</sup> )	Remarks <sup>a</sup>	
48	341.809836	58.116498	2007422604125045632	15.465 (0.004)	0.710	0.799	0.708	3.409	0.4231 (0.0258)	-2.5984 (0.028)	-2.069 (0.025)	MIR, TD
49	341.917174	58.151031	2007423050801656960	13.544 (0.005)	0.341	0.288	0.274	2.178	0.2133 (0.0124)	-3.1701 (0.013)	-1.777 (0.012)	MIR, TD
50	341.893151	58.090457	2007419644877416192	18.938 (0.010)	0.830	0.494	0.488	2.755	0.2933 (0.1346)	-2.3141 (0.146)	-2.162 (0.134)	MIR
51	341.503446	57.858029	2007409817998522368	...	1.331	1.178	0.709	2.590	...	...	...	MIR
52	341.636622	58.097843	2007417514575231232	...	0.860	0.459	0.675	2.768	0.5286 (0.2597)	-2.6819 (0.313)	-1.398 (0.289)	MIR
53	341.730776	57.953564	2007411952606264448	...	1.034	0.532	0.533	1.935	...	...	...	MIR
54	341.872801	58.088600	...	...	...	...	0.735	3.036	...	...	...	MIR

**Notes.**

<sup>a</sup> H $\alpha$ : H $\alpha$  emission line; NIR: near-infrared excess; MIR: mid-infrared excess; TD: transition disks.

<sup>b</sup> Parallax ( $\varpi$ ) negative values or high values.

<sup>c</sup> Proper motion suggesting non-membership.

## ORCID iDs

Tanvi Sharma  <https://orcid.org/0000-0003-1634-3158>  
 Wen Ping Chen  <https://orcid.org/0000-0003-0262-272X>  
 Neelam Panwar  <https://orcid.org/0000-0002-0151-2361>  
 Yan Sun  <https://orcid.org/0000-0002-3904-1622>  
 Yu Gao  <https://orcid.org/0000-0003-0007-2197>

## References

- Baade, D. 1983, *A&AS*, **51**, 235  
 Bailer-Jones, C. A. L., Rybizki, J., Fouesneau, M., Demleitner, M., & Andrae, R. 2021, *AJ*, **161**, 147  
 Beltrán, M. T., Massi, F., López, R., Girart, J. M., & Estalella, R. 2009, *A&A*, **504**, 97  
 Bertoldi, F. 1989, *ApJ*, **346**, 735  
 Bessell, M. S., & Brett, J. M. 1988, *PASP*, **100**, 1134  
 Bhatt, H., Pandey, J. C., Kumar, B., Sagar, R., & Singh, K. P. 2010, *NewA*, **15**, 755  
 Cantat-Gaudin, T., Jordi, C., Vallenari, A., et al. 2018, *A&A*, **618**, A93  
 Carpenter, J. M. 2001, *AJ*, **121**, 2851  
 Cernicharo, J., Bachiller, R., Duvert, G., Gonzalez-Alfonso, E., & Gomez-Gonzalez, J. 1992, *A&A*, **261**, 589  
 Chauhan, N., Pandey, A. K., Ogura, K., et al. 2009, *MNRAS*, **396**, 964  
 Chavarría-K., C., Moreno-Corral, M. A., Hernandez-Toledo, H., Terraneira, L., & de Lara, E. 1994, *A&A*, **283**, 963  
 Chen, W. P., Lee, H. T., & Sanchawala, K. 2007, in *IAU Symp. 237, Triggered Star Formation in a Turbulent ISM*, ed. B. G. Elmegreen & J. Palous (Cambridge: Cambridge Univ. Press), 278  
 Chen, W. P., Pandey, A. K., Sharma, S., et al. 2011, *AJ*, **142**, 71  
 Cohen, J. G., Frogel, J. A., Persson, S. E., & Elias, J. H. 1981, *ApJ*, **249**, 481  
 Conrad, C., Scholz, R. D., Kharchenko, N. V., et al. 2017, *A&A*, **600**, A106  
 Cutri, R. M., Skrutskie, M. F., van Dyk, S., et al. 2003, *VizieR On-line Data Catalog: II/246*  
 Cutri, R. M., Wright, E.L., Conrow, T., et al. 2013, *VizieR On-line Data Catalog: II/328*  
 Elmegreen, B. G. 1998, in *ASP Conf. Ser. 148*, ed. C. E. Woodward et al. (San Francisco, CA: ASP), 150  
 Elmegreen, B. G., & Lada, C. J. 1977, *ApJ*, **214**, 725  
 Gaia Collaboration 2020, *VizieR On-line Data Catalog: I/350*  
 Gandolfi, D., Alcalá, J. M., Leccia, S., et al. 2008, *ApJ*, **687**, 1303  
 Georgelin, Y. M., & Georgelin, Y. P. 1976, *A&A*, **49**, 57  
 Helou, G., & Walker, D. W. 1988, *IRAS Catalogs: The Small Scale Structure Catalog* (Washington, DC: GPO)  
 Hilditch, R. W., Harries, T. J., & Bell, S. A. 1996, *A&A*, **314**, 165  
 Israel, F. P. 1978, *A&A*, **70**, 769  
 Joncas, G., Dewdney, P. E., Higgs, L. A., & Roy, J. R. 1985, *ApJ*, **298**, 596  
 Joncas, G., Koempe, C., & de La Noe, J. 1988, *ApJ*, **332**, 1030  
 Joncas, G., & Roy, J. R. 1984, *ApJ*, **283**, 640  
 Karr, J. L., & Martin, P. G. 2003, *ApJ*, **595**, 900  
 Kharchenko, N. V., Piskunov, A. E., Röser, S., Schilbach, E., & Scholz, R. D. 2005, *A&A*, **438**, 1163  
 Koenig, X. P., & Leisawitz, D. T. 2014, *ApJ*, **791**, 131  
 Koenig, X. P., Leisawitz, D. T., Benford, D. J., et al. 2012, *ApJ*, **744**, 130  
 Lata, S., Pandey, A. K., Panwar, N., et al. 2016, *MNRAS*, **456**, 2505  
 Lee, H.-T., & Chen, W. P. 2007, *ApJ*, **657**, 884  
 Lee, H.-T., Chen, W. P., Zhang, Z.-W., & Hu, J.-Y. 2005, *ApJ*, **624**, 808  
 Leisawitz, D., Bash, F. N., & Thaddeus, P. 1989, *ApJS*, **70**, 731  
 Levreault, R. M. 1988, *ApJS*, **67**, 283  
 Meyer, M. R., Calvet, N., & Hillenbrand, L. A. 1997, *AJ*, **114**, 288  
 Moffat, A. F. J. 1971, *A&A*, **13**, 30  
 Morgan, L. K., Figura, C. C., Urquhart, J. S., & Thompson, M. A. 2010, *MNRAS*, **408**, 157  
 Morgan, L. K., Thompson, M. A., Urquhart, J. S., & White, G. J. 2008, *A&A*, **477**, 557  
 Morgan, L. K., Thompson, M. A., Urquhart, J. S., White, G. J., & Miao, J. 2004, *A&A*, **426**, 535  
 Ogura, K., Chauhan, N., Pandey, A. K., et al. 2007, *PASJ*, **59**, 199  
 Ogura, K., Sugitani, K., & Pickles, A. 2002, *AJ*, **123**, 2597  
 Pittard, J. M., & Stevens, I. R. 2002, *A&A*, **388**, L20  
 Ramesh, B. 1995, *MNRAS*, **276**, 923  
 Robitaille, T. P., Whitney, B. A., Indebetouw, R., & Wood, K. 2007, *ApJS*, **169**, 328  
 Samal, M. R., Pandey, A. K., Ojha, D. K., et al. 2012, *ApJ*, **755**, 20  
 Schwartz, P. R. 1987, *ApJ*, **320**, 258  
 Sharpless, S. 1959, *ApJS*, **4**, 257  
 Siess, L., Dufour, E., & Forestini, M. 2000, *A&A*, **358**, 593  
 Su, Y., Yang, J., Zhang, S., et al. 2019, *ApJS*, **240**, 9  
 Sugitani, K., Fukui, Y., Mizumi, A., & Ohashi, N. 1989, *ApJL*, **342**, L87  
 Sugitani, K., Fukui, Y., & Ogura, K. 1991, *ApJS*, **77**, 59  
 Sugitani, K., Tamura, M., & Ogura, K. 1995, *ApJL*, **455**, L39  
 Wilson, R. E. 1953, *GCRV*, 0